7-2009

Non-intrusive temperature measurement using microscale visualization techniques

Pramod Chamarthy
Purdue University - Main Campus

Suresh Garimella
School of Mechanical Engineering, sureshg@purdue.edu

Steven Wereley
Purdue University - Main Campus, wereley@purdue.edu

Experiments in Fluids 38 (2005) 90–98
DOI 10.1007/s00348-004-0895-y

Impact of hindered Brownian diffusion on the accuracy of particle-image velocimetry using evanescent-wave illumination

Reza Sadr, Haifeng Li, Minami Yoda

Abstract The "nano-particle image velocimetry" technique uses evanescent-wave illumination generated by total internal reflection at the wall to excite colloidal neutrally buoyant fluorescent tracer particles. The displacement of these particles over time as they are convected by the flow then gives the flow velocity components tangential to the wall. Since the extent of the illumination region normal to the wall is comparable to the particle diameter, a major source of error in this technique is particle "mismatch" within a pair of images due to Brownian diffusion causing a particle to move in to or out of the illuminated region. The "brightness" (proportional to the amount of imaged fluorescence) and size of individual particle images in nPIV data are discussed. A sequence of artificial nPIV images are generated for a known uniform velocity field with the particles subject to hindered Brownian diffusion. The velocity fields calculated from these artificial images are compared with the known velocity field to determine the effect of Brownian diffusion-induced particle mismatch on nPIV accuracy. A similar analysis is carried out for experimental nPIV images. The results provide design guidance for experimental measurements using the nPIV technique.

1 Introduction

Particle-image velocimetry (PIV) has been extensively used to measure nearly instantaneous velocity fields for more than a decade. To date, PIV remains the only experimental technique capable of measuring two components of the velocity over a two-dimensional plane or "slice" of flows ranging from creeping flow in microchannels (Meinhart et al. 1999) to supersonic flows in shock tubes (Haertig et al. 2002).

The rapid development of microfluidic devices fabricated with MEMS (microelectromechanical systems) technology has created a need for diagnostic tools with a spatial resolution of O (1 μm) and less. Micro-PIV (μPIV) is an extension of "classical" PIV to study flows at the microscale (Meinhart et al. 1999; Santiago et al. 1998). The major difference between μPIV and classical PIV is the method of illumination. In classical (mesoscale) PIV, the tracer particles are illuminated by a thin sheet of laser light and the out-of-plane spatial resolution (i.e., the resolution along the direction normal to the image plane), is set by the thickness of the laser sheet, typically 0.5–1 mm. Micro-PIV instead uses volumetric illumination, illuminating the entire volume of the microchannel with, for example, a laser beam.

Meinhart et al. (2000a) suggested that the out-of-plane spatial resolution of μPIV is determined by the depth of focus of the imaging system. Olsen and Adrian (2000a) showed that this resolution is more accurately estimated by the "depth of correlation," an experimental parameter describing the extent over which tracer particles significantly contribute to the measured velocity. This parameter is a function of the particle size and various imaging system characteristics. At present, the best reported out-of-plane resolution for μPIV is, to our knowledge, about 1.8 μm for velocity results obtained at least 450 nm away from the wall (Tretheway and Meinhart 2002).

This volumetric illumination introduces errors unique to μPIV. First, all particles within the entire illuminated region (i.e., the cone of illumination) contribute to the recorded image, irrespective of whether they are in or out of focus. Particles that are out of focus therefore increase the background noise level, which reduces the signal to noise ratio (SNR) of the image. Meinhart et al. (2000a) showed that SNR for μPIV data can be as low as unity if the experimental parameters are not chosen "judiciously." Moreover, both the diameter and intensity of a particle image vary with distance of that particle from the focal plane. Even particle tracer images that are considered "in focus" (i.e., within the depth of field) have different contributions to the cross-correlation peak depending upon their location with respect to the focal plane, introducing errors in μPIV results. Olsen and Adrian (2000b) coined a new parameter, the "particle visibility," defined as the ratio of the peak intensity of a particle image considered in focus to the background intensity, and showed that this parameter was a strong function of the focal number of the imaging system, the extent of the microchannel normal to the image plane, and the particle diameter and concentration. They further indicate that even particles that are out of focus still have an effect on the correlation peak and therefore contribute to the measured velocity. They therefore introduced the "depth of correlation" as a measure of the out-of-plane resolution. The analytical

Received: 25 March 2004 / Accepted: 29 September 2004
Published online: 23 November 2004

R. Sadr (✉), H. Li, M. Yoda
G. Woodruff School of Mechanical Engineering,
Georgia Institute of Technology, Atlanta,
GA 30332-0405, USA
E-mail: reza.sadr@me.gatech.edu

results of Olsen and Adrian (2000b) were experimentally verified by Bourdon et al. (2004).

Brownian diffusion is also an important issue in μPIV because the technique uses colloidal tracers with typical diameters of 100–500 nm and because the velocities in liquid microflows are usually less than O (0.1 mm/s). Santiago et al. (1998) gave a first-order estimate for the error due to unconfined Brownian diffusion of particles in a μPIV experiment and noted that the error due to the Brownian diffusion imposes a practical lower limit on both the time interval between images within an image pair and the tracer particle diameter for a given accuracy. Olsen and Adrian (2000b), who further investigated the effect of Brownian motion on cross-correlation PIV, showed that Brownian diffusion reduced the height of the correlation peak by a factor they called the "Brownian motion parameter." Although they reported that this parameter is difficult to quantify in μPIV applications because the particle image diameter varies throughout the measurement volume due to the volumetric illumination and out-of-focus particles associated with the technique, their results indicate that Brownian motion imposes a bias on μPIV velocity data. Olsen and Adrian (2000b) also showed that the Brownian motion serves to increase the depth of correlation thus increasing bias due to velocity gradient.

We have recently developed a new technique, nanoparticle image velocimetry (Zettner and Yoda 2003; Sadr et al. 2004) for near-wall velocimetry. Unlike μPIV, the technique uses evanescent-wave illumination generated by total internal reflection (TIR) at the interface between the wall and the fluid; the evanescent wave typically illuminates only a portion of the microchannel. Because nPIV is inherently limited to velocity measurements in the near-wall region over a distance comparable to the illumination wavelength, the technique complements the bulk flow velocimetry capabilities of μPIV. The out-of-plane spatial resolution of nPIV is determined by the larger of two factors, namely the penetration depth of the evanescent wave and the tracer particle diameter. Given that this resolution is typically O (100 nm), Brownian diffusion—and, more specifically, particle mismatch between the two images within the pair due to hindered Brownian diffusion—is an even more important issue for nano-(vs. micro-)PIV.

This work is the first analysis of how Brownian diffusion of the colloidal particle tracers affects the accuracy of nPIV data and incorporates the effects due to nonuniform evanescent-wave illumination. A simple model is presented in Section 2 of the total fluorescence emitted by a colloidal particle illuminated by an evanescent wave and detected by an imaging system. Section 3 describes the Monte Carlo simulations used to generate artificial nPIV images with a known uniform displacement and Brownian diffusion coefficient. Section 4 presents and discusses the results from processing these artificial images using standard cross-correlation PIV techniques and the errors due to Brownian diffusion. Finally, experimental nPIV images obtained for a steady and uniform electroosmotic flow are processed using the same parameters and techniques. The errors due to Brownian diffusion-induced particle mismatch are estimated and discussed.

2 Evanescent-wave illumination of spherical particles

Unlike the volumetric illumination used in μPIV, nPIV uses evanescent-wave illumination to interrogate the near-wall region of the flow. This evanescent wave has an intensity that decays exponentially with distance normal to the wall with a characteristic length, the penetration depth, typically smaller than the illumination wavelength. This penetration depth is much less in most cases than the depth of focus of the imaging system. Unlike μPIV, the nPIV particle images are therefore all in focus with no background noise from out-of-focus tracers. In this Section, the characteristics of the particle image that affect the cross-correlation peak, namely its brightness and size, are discussed. A simple model is presented of the brightness of, or the power emitted by, fluorescent spherical particles illuminated by an evanescent wave.

In a nPIV image, total internal reflection fluorescence microscopy is used to image tracer particles in the near-wall region. When a light beam propagating through a transparent medium with a higher refractive index n_2 (e.g. glass) encounters an interface with a medium of lower refractive index n_1 (e.g. water), it undergoes total internal reflection (TIR) for angles of incidence (measured from the normal to the interface) exceeding the critical angle $\theta_c=\sin^{-1}(n_1/n_2)$. Some of the incident energy, however, penetrates into the less dense medium (with refractive index n_1). This so-called "evanescent wave" propagates parallel to the interface with an intensity that decays exponentially with distance normal to and measured from the interface z:

$$I(z) = I_o exp\left\{-\frac{z}{z_p}\right\} \tag{1}$$

where I_o is the intensity at the interface (z=0) and the penetration depth

$$z_p = \frac{\lambda_o}{4\pi n_2}\left[sin^2\theta - \left(\frac{n_1}{n_2}\right)^2\right]^{-1/2}. \tag{2}$$

Here, λ_0 is the wavelength of the illumination in vacuum and θ is the angle of incidence.

A fluorescently labeled molecule or particle illuminated by the evanescent wave will absorb energy from this wave and emit longer-wavelength fluorescence. This phenomenon is the basis of the total internal reflection fluorescence (TIRF) microscopy technique used commonly in biophysics (Axelrod 2001). Figure 1 shows a fluorescent sphere of radius a illuminated by an evanescent wave with penetration depth z_p (note: $a \sim z_p$) whose center and edge are at distances z' and $h = z' - a$ from the wall, respectively.

Assuming that: (1) this sphere is opaque and that only the fluorophores on the surface of the sphere are excited by the illumination; (2) the presence of the sphere has a negligible effect upon the evanescent wave (note that only a single "layer" of spheres are illuminated, since $z_p \sim 2a$ and interparticle interactions are negligible for low tracer seeding densities); and (3) the intensity I_0 is constant, the net power emitted by this sphere illuminated by the

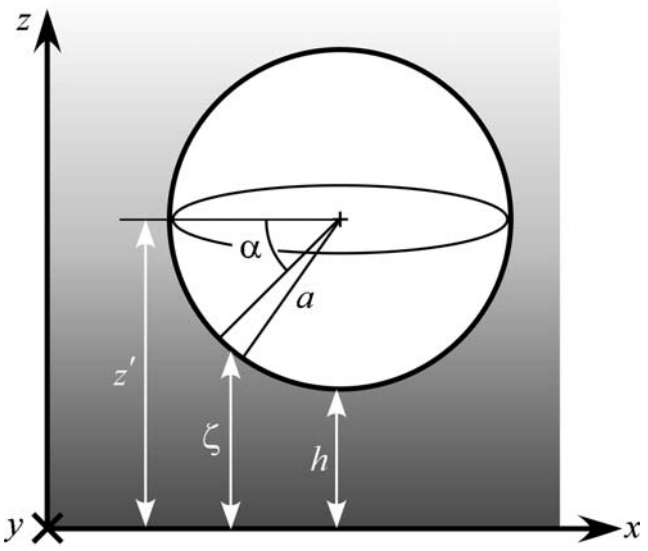

Fig. 1. A spherical particle illuminated by an evanescent wave. The Cartesian coordinate system is defined so that the x - and z -axes are parallel and normal to the wall, respectively, and the y-axis is parallel to the wall and orthogonal to x

evanescent wave and collected by a microscope objective–the "brightness"—should be proportional to the product of the evanescent-wave intensity and the surface area of the sphere. Since the evanescent-wave intensity is only a function of z, the energy emitted by the thin ring spanning an angle da on the surface of this sphere centered about z=ζ=z′-a sin α is then $I(\zeta)$dA where the area of the ring

$$dA = 2\pi a^2 cos\alpha \, d\alpha = -2\pi a \, d\zeta.$$

A fraction of this fluorescence is then collected by a microscope objective placed below the sphere. Assuming therefore that only the light emitted by the bottom half of the sphere facing the wall is collected, the total energy detected by the imaging system should be proportional to the net power emitted by the bottom half of the sphere:

$$B = K \int_{\alpha=0}^{\alpha=\pi/2} I(\zeta)\, dA = K 2\pi a I_o \int_{h}^{z'} exp\left\{-\frac{\zeta}{z_p}\right\} d\zeta. \qquad (3)$$

where K is the "collection efficiency," or the fraction of the fluorescence collected by the objective. Given that both the particles and the penetration depth are orders of magnitude smaller than the aperture of the objective, we assume that the fraction of the light emitted from particle tracers in the evanescent wave that is collected by the objective is constant. Integrating and simplifying gives

$$B = K \cdot B_o exp\left\{-\frac{h}{z_p}\right\} \qquad (4)$$

where

$$B_o = 2\pi z_p^2 I_o \left[\frac{a}{z_p}\left(1 - exp\left\{-\frac{a}{z_p}\right\}\right)\right] \qquad (5)$$

is the net power emitted by the (bottom half of) the particle when it is in contact with the wall, or $h = 0$.

Equation (4) shows that the total power emitted by—or the "brightness" of—a spherical particle illuminated by an evanescent wave also decays exponentially with its distance from the wall (albeit measured from its nearest edge).

In addition to the brightness of the particle image, the size of the particle image also affects the cross-correlation peak. Nano-(and micro-)PIV both use tracers where a is typically less than the illumination wavelength and image the tracers with microscopes. For a particle in "perfect" focus (i.e., at the focal plane), the actual image recorded on a CCD camera coupled to the microscope is then the convolution of the geometric and diffraction-limited images. Assuming that the geometric and diffraction-limited images are both Gaussian, the resulting convolution is a Gaussian function with an effective diameter (Adrian 1991)

$$d_e = \left[4M^2a^2 + d_{s\infty}^2\right]^{1/2} \qquad (6)$$

where M is the magnification of the microscope objective and $d_{s\infty}$ is the diffraction-limited diameter for an infinity-corrected optical system. Meinhart and Wereley (2003) showed that

$$d_{s\infty} = 1.22\, M\lambda \left[\left(\frac{n_o}{NA}\right)^2 - 1\right]^{1/2}. \qquad (7)$$

Here, λ is the wavelength of the light emitted by the particle, n_0 is the refractive index of the immersion medium between the microscope objective and the object, and NA is the numerical aperture of the objective.

3 Generation of artificial images

Artificial nPIV images with a known uniform displacement and grayscale characteristics similar to actual experimental images were generated as described in this Section. Monte Carlo simulations were used to create a random ensemble of particle locations; the position of these particles after some time interval was then calculated for uniform steady flow using the Langevin equation with hindered Brownian diffusion coefficients.

An ensemble of 5,000 particle image pairs was generated for a range of time intervals Δt where $0 \le \Delta t \le 14$ ms. About 600 particles are initially scattered randomly over a volume with dimensions of 110 μm×18.3 μm×0.45 μm ($x \times y \times z$); the z -dimension of this volume corresponds to about 5 z_p . The particle volume concentration is about 0.03%. In all cases, $z'/a > 1$. Most of the image parameters used here were chosen to match those in our previous nPIV study of steady fully-developed electroosmotic flow for thin electric double layers (Sadr et al. 2004)

The first image in each pair is constructed by creating a 640×100 pixel array with background noise with a grayscale histogram comparable to that obtained for experimental nPIV images. Grayscale images of particles within this 640×100 pixel ($x \times y$) field of view are then added to this array centered in the initial volume. Since the tracers in nPIV are all in "perfect" focus, Eq. (6) is used to

estimate the particle image size, which is constant under our assumptions of a fixed optical magnification and monodisperse tracers. Variations in particle image size in nPIV images are therefore primarily due to variations in the particle image intensity due to the exponential decay of the evanescent-wave illumination; in these artificial images, a Gaussian intensity distribution was assumed with the peak grayscale value calculated using Eq. (4).

The particle number density, particle image shape and background noise characteristics are adjusted so that the image characteristics match those for a typical experimental nPIV image following the guidelines suggested by Westerweel (2002). Figure 2 shows representative artificial and experimental nPIV images.

For the second image, the particles in the first image are displaced by the given velocity field and Brownian diffusion. Brownian movement of the submicron tracer particles in the illuminated region is an important source of error since $a \sim z_p$ in nPIV. The displacements are determined using the Langevin equation, which is the standard equation of motion for a colloidal particle undergoing Brownian diffusion. Specifically, Langevin-type equations describe the temporal change in acceleration due to a stochastic force. The Brownian displacement vector, Δr_B, of the spherical particle over the time interval Δt is calculated using the Langevin equation under the assumptions of Stokes flow and Brownian diffusion (Clark et al. 1987):

$$\Delta r_B = \sum \{(\nabla \cdot D)\ \delta t + \chi\ \delta r\} \tag{8}$$

where D is the Brownian diffusion coefficient tensor, χ is a sequence of normally distributed random numbers whose mean is zero and standard deviation is equal to unity and δr is the rms displacement due to Brownian diffusion over the interval $\delta t \ll \Delta t$.

The first term on the right-hand side of the equation, the gradient term, accounts for any spatial dependence in the diffusion coefficient. Since hindered Brownian diffusion (unlike Brownian diffusion in an infinite domain) depends upon distance from the wall, this term is nonzero and must be included in the Brownian displacement for this case. When solving Eq. (8), the time step δr is subject to two constraints. First, $\delta t \ll \tau_p$ where the particle relaxation time for a particle of mass m is:

$$\tau_p = \frac{m}{6\pi\mu a} \tag{9}$$

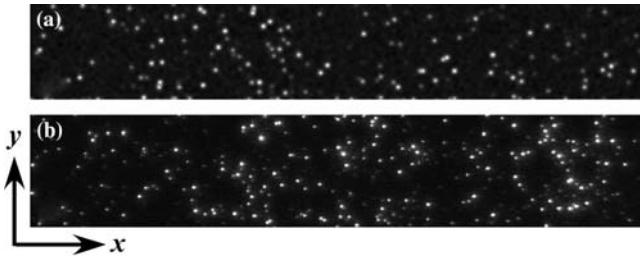

Fig. 2. Typical artificial (*a*) and experimental (*b*) nPIV images

For submicron latex particles with a specific gravity of 1.05, τ_p =0 (10^{-9} s). Second, δt should remain small enough so D remains essentially constant during the time step. Here, δt was chosen to be 50 μs.

The next term in this equation is the contribution due to random Brownian motion. For time intervals δt much larger than the particle relaxation time τ_p, the rms displacement due to Brownian diffusion is estimated by

$$\delta r = \sqrt{2D\,\delta t}. \tag{10}$$

For a particle in an unconfined flow the Brownian diffusion coefficient is a scalar given by the Stokes-Einstein equation (Einstein 1905):

$$D_\infty = \frac{kT}{6\pi\mu a} \tag{11}$$

where k is the Boltzmann constant and T and μ are the fluid absolute temperature and viscosity, respectively.

When a particle is close to a wall, its diffusion is reduced or hindered by an additional hydrodynamic drag due to the wall. Although these hindered diffusion coefficients are different for motion normal and parallel to the wall, both diffusion coefficients tend to vanish as the sphere approaches the wall and tend to the Stokes-Einstein value as the particle moves away from the wall. The diffusion coefficient tensor

$$D = D_\infty \begin{bmatrix} \beta_\parallel & 0 & 0 \\ 0 & \beta_\parallel & 0 \\ 0 & 0 & \beta_\perp \end{bmatrix} \tag{12}$$

where β is a correction factor incorporating wall effects and the subscripts $\parallel$ and $\perp$ denote motion parallel and perpendicular to the wall, respectively.

Bevan and Prieve (2000) showed that $\beta\ \perp$, the correction factor for motion perpendicular to the wall, can be approximated as

$$\beta_\perp = \frac{6h^2 + 2ah}{6h^2 + 9ah + 2a^2}.$$

where h is the distance between the plane surface and the nearest edge of the particle (cf. Fig. 1). Faxén (1922) showed that $\beta_\parallel$ can be expressed as a power series in (a/z) where z is the distance between the plane surface and the center of the particle ($z = h + a$); for Stokes flow (Clark et al. 1987)

$$\beta_\parallel = 1 - \frac{9}{16}\left(\frac{a}{z}\right) + \frac{1}{8}\left(\frac{a}{z}\right)^3 - \frac{45}{256}\left(\frac{a}{z}\right)^4 - \frac{1}{16}\left(\frac{a}{z}\right)^5.$$

The rms displacement due to hindered Brownian diffusion is therefore estimated along the directions parallel and perpendicular to the wall using Eq. (10) and the diffusion tensor given by Eq. (12).

Figure 3 shows particle trajectories in water at T=300K over an interval Δt=2ms (40 δt) for an a =50 nm particle starting near the wall. This figure compares the trajectories of the particle using δr calculated using Eq. (10) and D_∞ (*a*), Eq. (10) and the hindered diffusion coefficients given by Eq. (12) (*b*), and Δr_B calculated using Eqs. (8) and (12) (*c*). The same "random" number χ was used for all three

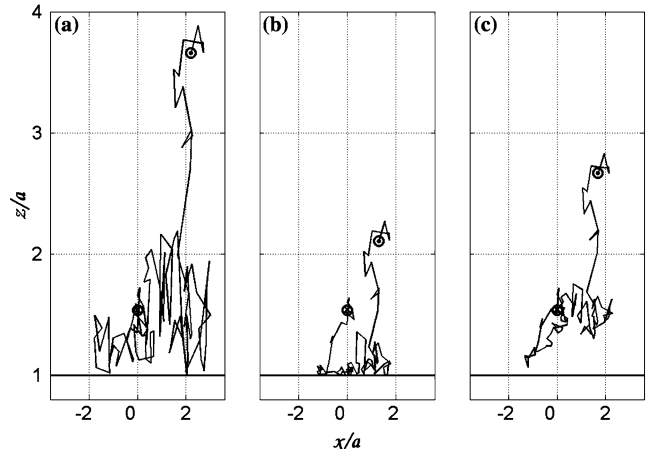

Fig. 3. A projection of particle trajectories onto the x-z plane for a =50 nm. In all cases, the particle center starts at the same position near a solid wall (⊗) and its motion is calculated using: (*a*) Eq. (10) and D_∞, (*b*) Eqs. (10) and (12), and (*c*) Eq. (8). The endpoint of the particle trajectory is denoted by ⊙

cases at each time step δt. The trajectories shown here are therefore identical except for the different models used to simulate Brownian diffusion. In these simulations, we use a particle "wall interaction model" that assumes the particle interacts with the wall when $z'/a \leq 1$ via perfectly elastic collision. As expected, the figure and several other simulations (not shown here) show that the presence of the wall hinders the particle motion. The figure also demonstrates, however, that the gradient term in the Langevin equation increases the overall particle mobility in this near-wall region, and therefore cannot be ignored.

Consider the trajectory of a particle whose center is initially at a position $1 < z'/a < \Pi$ over Δt =6 ms (300 δt). The Brownian diffusion coefficient for each particle can be calculated either by ensemble averaging the diffusion coefficients calculated using Eq. (12) for each z-location of the particle center over time (D) or directly from the actual particle displacement (**D**). The latter directly accounts for the wall interaction model used here. Table 1 shows the results (normalized by D_∞) averaged over the 10^5 particles in each simulation. The diffusion coefficients for motion perpendicular and parallel to the wall denoted again by the subscripts $\perp$ and $\|$, respectively. As expected, the average Brownian diffusion in the wall region increases with Π, or as the particle becomes less "hindered," with $D_\| > D_\perp$. Not surprisingly, particle motion normal to the wall is considerably affected by the wall interaction model used here, with $\mathbf{D}_\perp > D_\perp$; motion parallel to the wall is essentially unaffected, however, with $\mathbf{D}_\| \approx D_\|$.

Table 1. Comparison of average Brownian diffusion coefficients for particles starting at $1< z'/a <\Pi$

Π	$D_\|/D_\infty$	$\mathbf{D}_\|/D_\infty$	$D_\perp/D_\infty$	$\mathbf{D}_\perp/D_\infty$
3	0.774	0.774	0.582	0.261
5	0.804	0.805	0.637	0.353
7	0.829	0.827	0.683	0.440
9	0.849	0.847	0.720	0.516
11	0.865	0.865	0.750	0.578

4 Results

A FFT correlation-based interrogation algorithm (Liang et al. 2002) and a Gaussian peak-finding algorithm based upon using a Gaussian surface fit over at least 11 points (above the noise level) were used to obtain particle displacement vectors from pairs of artificial images. A relatively large interrogation window size of 118×98 pixels was chosen to ensure that each window contained at least 30 tracer particles. The overlap between interrogation windows was 50%. Most of the processing parameters used here were chosen to match those used in our previous experimental nPIV study (Sadr et al. 2004). The results are then compared with the known displacement to determine the displacement error averaged over the 5,000 pairs in each dataset.

Like μPIV, Brownian diffusion of the particle tracers parallel to the wall has a minimal effect upon the accuracy of the nPIV technique. Using the averaged diffusion coefficient values given in Table 1 and Eq. (10), an a=50 nm particle tracer starting at π=3 has a rms displacement of $\Delta x \sim \Delta y$=218 nm and Δz =189 nm. For the nPIV optical setup used by Sadr et al. (2004), this Brownian motion corresponds to an in-plane displacement of about one pixel. The stochastic Brownian displacements can essentially be minimized either by averaging the cross-correlations over several realizations or by using larger interrogation windows containing larger number of tracer particle images.

Unlike μPIV, however, Brownian diffusion perpendicular to the wall plays a major role on the accuracy of nPIV results because of the relatively thin ($a \sim z_p$) region illuminated by the evanescent wave and its exponentially decaying intensity. Diffusion perpendicular to the wall causes "particle mismatch," where the tracers leave ("drop out") or enter ("drop in") the region illuminated by the evanescent wave within the image pair, affecting the SNR of the cross-correlation peak. Figure 4 shows the fraction

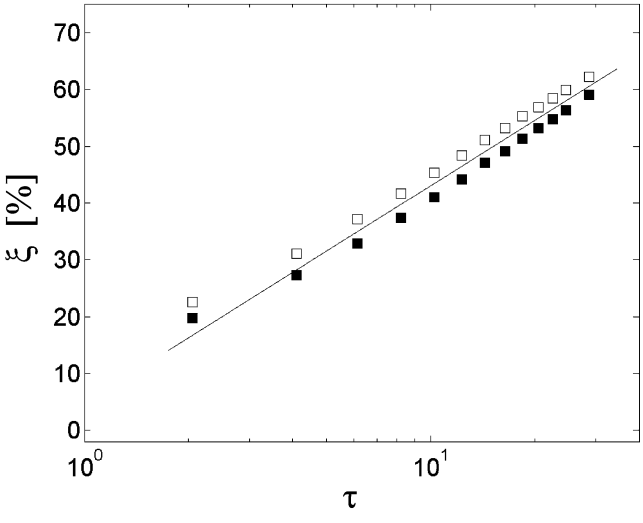

Fig. 4. Fraction of mismatched particles as a function of normalized time delay within the image pair. Open and closed symbols denote results for unconfined and hindered Brownian diffusion, respectively, in this and following figures

of mismatched particles (vs. the total number of particles), ξ , within an image pair as a function of the time interval within the image pair normalized by the Brownian time scale

$$\tau = \frac{\Delta t}{a^2/D_\infty}$$

for both unconfined (open symbols) and hindered (closed symbols) Brownian diffusion. Strictly speaking, the Monte Carlo simulations track "matched" particles within the image pair by identifying particles that are present in both images within the pair. A particle is considered to be "present" when its peak intensity exceeds the noise level in the image. The number of mismatched particles is then the number of matched particles subtracted from the total number of particles in the first image; note that the total number of particles per image is essentially constant within the image pair. The plot shows that ξ increases nearly logarithmically with τ, and that the presence of the wall reduces the amount of particle mismatch by about 5%. The rest of the results are presented as a function of this fraction of particle mismatch. Although this analysis assumes colloidal particle tracers and exponentially decaying illumination, the results should also be qualitatively applicable to other types of particle mismatch due, for example, to strong out-of-plane flow.

Figure 5 shows the average displacement error, ϵ, as a function of ξ. Surprisingly, this error is essentially constant and well below the typical accuracy of PIV algorithms of about 0.05 pixels (Raffel et al. 1998) for ξ<45%. As expected, ϵ for both hindered and unconfined Brownian diffusion show similar trends. Note that with at least 30 tracer particles per interrogation window, 45% particle mismatch corresponds to at least 16 "matched" particles in both images within the pair.

Figure 6 shows the standard deviation of the displacement error (over 5,000 realizations), ϵ' on a logarithmic scale as a function of ξ. The scatter in the displacement error is at least one order of magnitude more than the mean. Also, ϵ' grows exponentially as ξ increases, and the rate of growth doubles for ξ> 45%.

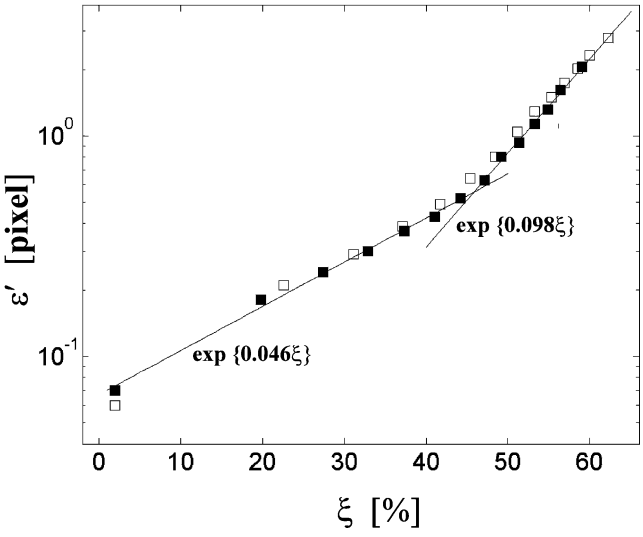

Fig. 6. Standard deviation of the displacement error as a function of the fraction of mismatched particles. The solid lines are the exponential functions indicated on the Figure

The increase in both ϵ and ϵ' is due to a decrease in the SNR and an increase in the width of the cross-correlation peak used to find the particle displacement (and hence velocity). Figure 7 shows the SNR of the cross-correlation peak, defined here as the ratio of peak to the background correlation noise level, as a function of the fraction of mismatched particles ξ. The SNR decreases monotonically as ξ increases, in agreement with the analytical results of Olsen and Adrian (2000b), which showed that an increase in Brownian motion reduces the SNR of the PIV correlation peak. Moreover, SNR decreases essentially linearly as ξ increases for ξ> 40% (as indicated by the solid line in the figure). This decrease in SNR increases the number of spurious displacement vectors.

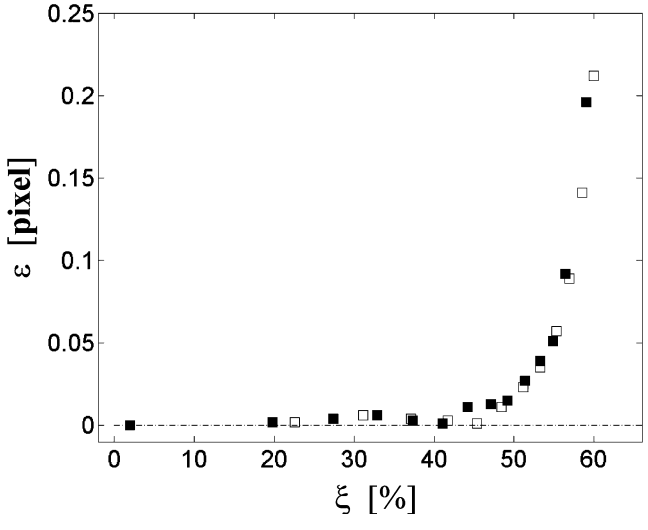

Fig. 5. Average displacement error as a function of the fraction of mismatched particles

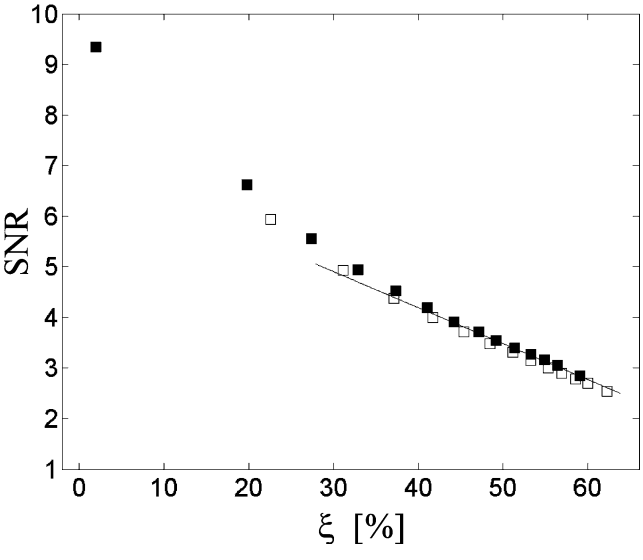

Fig. 7. The averaged height of the correlation function as a function of the fraction of mismatched particles

Figure 8, a graph of the width of the correlation function W as a function of ξ, shows that the width of the correlation peak increases even more rapidly than its height, as indicated by the SNR (cf. previous figure). Here, W is calculated by fitting a Gaussian function ($\propto \exp\{-x^2+y^2)/W^2\}$) to the cross-correlation peak. This increase in W reduces the peak-finding accuracy and hence the sub-pixel accuracy of the nPIV results.

The results from the analysis of these synthetic images have a number of implications for the accuracy of the experimental nPIV results. As Brownian motion becomes more significant, the nPIV results become less accurate due to both an increase in width and decrease in height of the cross-correlation peak. Reducing the time delay Δt within the nPIV image pair will reduce Brownian effects and hence increase accuracy, but if Δt is too small, the particle displacement within the image pair becomes very small (compared with the particle image size). This can lead to undesirably large measurement errors since this error is inversely proportional to the magnitude of particle displacement. Brownian effects can also be reduced by using larger tracer particles (i.e., increasing a), but this increases the (usually out-of-plane) spatial resolution of the nPIV data.

The effects of Brownian motion on both the height and width of the cross-correlation peak in nPIV agree with the trends predicted by the analysis of Olsen and Adrian (2000b) for μPIV. In addition, the analytical results of Olsen and Bourdon (2003) also indicate that in μPIV the out-of-plane motion of the tracer particles due to the fluid velocity will reduce the height of the correlation peak. The effects of Brownian motion on nPIV data are therefore qualitatively similar to those observed in μPIV, despite their differences in terms of hindered (vs. unconfined) diffusion and out-of-plane spatial resolution comparable to (vs. much greater than) tracer particle diameter.

As mentioned previously, this study used a base interrogation window size of 118×98 pixels, corresponding in the experimental study described in Sadr et al. (2004) to an in-plane spatial resolution of 20×16 μm. For a given optical magnification, decreasing the interrogation window size enhances the in-plane spatial resolution but decreases the number of tracers per interrogation window. Figure 9 shows the effect of the number of particles in the interrogation window on the nPIV error estimation for image pairs with a particle number density of 3.1×10^{-3} particles/pixel and a time interval τ =12.3 (Δt =6 ms) within the pair. The figure shows ϵ (squares) and ϵ' (circles), both normalized by their values for the base interrogation window (denoted by the subscript 0) on a logarithmic scale as a function of the number of particles N normalized by the number of particles in the base window N_0. Both ϵ and ϵ' increase exponentially as N / N_0 decreases for values below unity. For N / N_0=0.2, corresponding to the smallest interrogation window considered here of 60×40 pixels (where there were at least four matched particles in the image pair), ϵ=0.37 pixels and ϵ'=3.6 pixels. Note that ensemble averaging of the cross-correlation, which has been used to reduce interrogation window size while maintaining reasonable accuracy for μPIV measurements in steady flows (Meinhart et al. 2000b), can also be used for nPIV measurements of steady flows to reduce such errors.

Finally, this type of analysis can also be applied to experimental images. Figure 10 shows the average bulk velocity U measured by the nPIV technique as a function of driving external electric field E for steady and fully developed electroosmotic flow (EOF) of an aqueous 3.6 mM sodium tetraborate solution through a fused silica microchannel with a nominally rectangular cross-section of dimensions 24.7 μm×51.2 μm. Further experimental details are given in Sadr et al. (2004). The experimental images using FFT-based correlation and an interrogation window size of 118×98 pixels. These nPIV results are therfore slightly different from the results given in Sadr et al. (2004), which were calculated using the EdPIV package (Wereley et al. 2002). Nevertheless, the average error (95% confidence level) for a single velocity vector at a given location—which reflects the mean in-plane

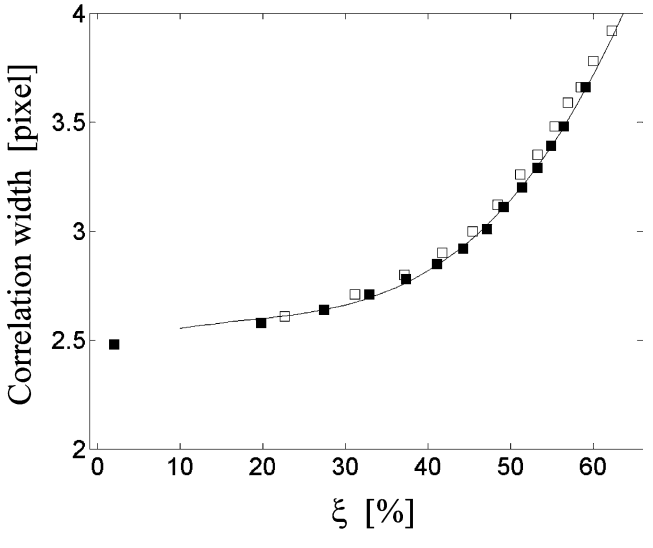

Fig. 8. Width of the correlation function (based upon a Gaussian function curve-fit) as a function of the fraction of mismatched particles. The solid line represents a third-order polynomial in ξ

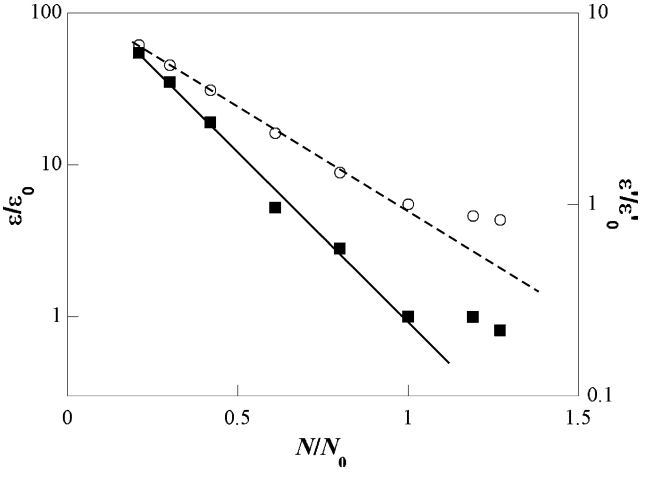

Fig. 9. The effect of the number of tracers in the interrogation window on the calculated error

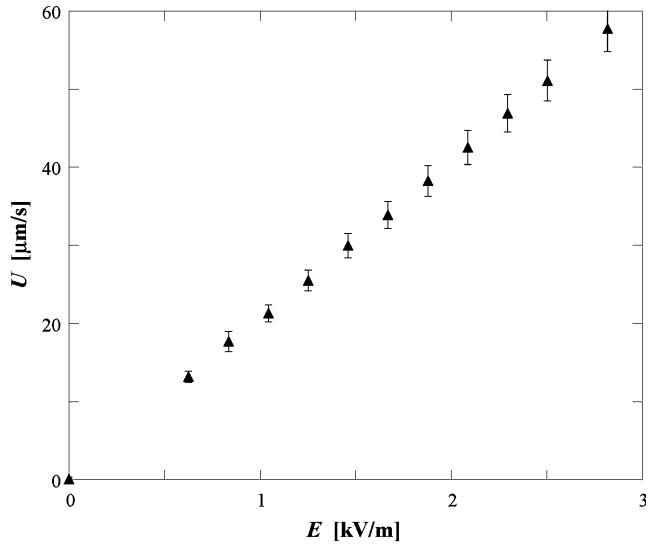

Fig. 10. Plot of average bulk velocity U as a function of driving external electric field E for steady and fully developed EOF through a 24.7-μm rectangular channel

Brownian diffusion for all tracer particles within the interrogation window—over 999 relizations is typically 6%. After spatial and temporal averaging, this error accounts for about 2% of the 95% confidence intervals given in Fig. 10. Imaging errors—due to the limiting spatial resolution of the CCD camera and uncertainties in determining the magnification, for example—are a much larger source of error than Brownian diffusion-induced particle mismatch in these experimantal data. Given that the time interval between images Δt=6.5 ms (τ=13.3), the fraction of mismatched particles ξ=45% (*cf.* Fig. 4). The relatively minor errors due to Brownian diffusion-induced particle mismatch in the experimental data are therefore in agreement with the results of Fig. 5.

5 Conclusions

The impact of Brownian diffusion-induced particle mismatch on the accuracy of nPIV data was quantified using artificial images. Significant efforts were made to ensure that the artificial images were accurate representations of previous experimental images obtained for steady and fully-developed electroosmotic flow through rectangular microchannels. Tracer particle positions for the artificial images were generated using Monte Carlo simulations. The tracers were then advected for a prespecified uniform velocity field using the Langevin equation and hindered Brownian diffusion coefficients. Particle interactions with the wall were modeled as perfectly elastic collisions. Tracer images were calculated for particles illuminated by evanescent waves with exponentially decaying intensity. A simple analysis shows that the power emitted by a spherical particle illuminated by evanescent waves and imaged from below also decays exponentially with its distance from the wall measured from the nearest edge. Finally, the noise and background characteristics of the artificial images were adjusted so that their histograms were similar to those for the experimentally obtained images.

Comparisons of the velocity fields obtained from the artificial images with known values demonstrate that the error is essentially constant and negligible compared with typical PIV errors for up to about 45% particle mismatch. In other words, only slightly more than half the tracers in the first image should be present in the second image within the pair for the relatively large interrogation windows used here containing at least 30 tracer particles. Above 45% particle mismatch, the error increases rapidly due to both a decrease in the height and an increase in the width of the correlation peak. The interrogation window size has a major impact upon the accuracy of nPIV data, with error increasing exponentially with decreasing window size and hence number of tracers per window. Analysis of experimental nPIV images using identical parameters suggests that the errors due to Brownian diffusion-induced particle mismatch are negligible compared with various experimental errors such uncertainties in estimating magnification and the discretization of the image by the CCD array.

This study was intended to provide design guidance for nPIV experiments; the results were therefore obtained for conditions typical of nPIV. Nevertheless, these results should also provide qualitative insight into how particle mismatch due to phenomena other than Brownian diffusion such as strongly three-dimensional flow affects the accuracy of PIV measurements. We plan next to analyze how shear (i.e., nonuniform flow velocities) affects the accuracy of nPIV data.

References

Adrian RJ (1991) Particle-imaging techniques for experimental fluid mechanics. Ann Rev Fluid Mech 23:261–304

Axelrod D (2001) Total internal reflection fluorescence microscopy in cell biology. Traffic 2:764–774

Bevan MA, Prieve DC (2000) Hindered diffusion of colloidal particles very near to a wall: revisited. J Chem Phys 113:1228–1236

Bourdon CJ, Olsen MG, Gorby AD (2004) Validation of an analytical solution for depth of correlation in microscopic particle image velocimetry. Meas Sci Technol 15:318–327

Clark AT, Lal M, Watson GM (1987) Dynamics of colloidal particles in vicinity of an interacting surface. Faraday Discuss Chem Soc 83:179–191

Einstein A (1905) Über die von der molekularkinetischen Theorie der Wärme geforderte Bewegung von in ruhenden Flüssigkeiten suspendierten Teilchen. Ann Phys 17:549

Faxén H (1922) Der Widerstand gegen die Bewegung einer starren Kugel in einer zähen Flüssigkeit, die zwischen zwei parallelen Ebenen Wänden eingeschlossen ist. Ann Phys 4(68):89–119

Haertig J, Havermann M, Rey C, George A (2002) Particle image velocimetry in Mach 3.5 and 4.5 shock-tunnel flow. AIAA J 40:1056–1060

Liang DF, Jiang CB, Li YL (2002) A combination correlation-based interrogation and tracking algorithm for digital PIV evaluation. Exp Fluids 33:684–695

Meinhart CD, Wereley ST (2003) The theory of diffraction-limited resolution in micro-particle image velocimetry. Meas Sci Technol 14:1047–1053

Meinhart CD, Wereley ST, Gray MHB (2000a) Volume illumination for two-dimensional particle image velocimetry. Meas Sci Technol 11:809–814

Meinhart CD, Wereley ST, Santiago JG (1999) PIV measurement of a microchannel flow. Exp Fluids 27:414–419

Meinhart CD, Wereley ST, Santiago JG (2000b) A PIV algorithm for estimating time-averaged velocity fields. Trans ASME: J Fluids Eng 122:285–289

Olsen MG, Adrian RJ (2000a) Out-of-focus effects on particle image visibility and correlation in microscopic particle image velocimetry. Exp Fluids 29:S166–S174

Olsen MG, Adrian RJ (2000b) Brownian motion and correlation in particle image velocimetry. Opt Laser Technol 32:621–627
Olsen MG, Bourdon CJ (2003) Out-of-plane motion effects in microscopic particle image velocimetry. J Fluids Eng 125:895–901
Raffel M, Willert C, Kompenhans J (1998) Particle image velocimetry; a practical guide. Springer, Berlin Heidelberg New York
Sadr R, Yoda M, Zheng Z, Conlisk AT (2004) An experimental study of electro-osmotic flow in rectangular microchannels. J Fluid Mech 506:357–367
Santiago JG, Wereley ST, Meinhart CD, Beebe DJ, Adrian RJ (1998) Particle image velocimetry system for microfluidics. Exp Fluids 25:316–319
Tretheway DC, Meinhart CD (2002) Apparent fluid slip at hydrophobic microchannel walls. Phys Fluids 14:L9–L12
Wereley ST, Gui L, Meinhart CD (2002) Advanced algorithms for microscale particle image velocimetry. AIAA J 40:1047–1055
Westerweel J (2000) Theoretical analysis of the measurement precision in particle image velocimetry. Exp Fluids 29:S3–S12
Zettner CM, Yoda M (2003) Particle velocity field measurements in a near-wall flow using evanescent wave illumination. Exp Fluids 34:115–121